SCIENTIFIC REPORTS

OPEN

SUBJECT AREAS:
PHOTOCATALYSIS
SOLID-PHASE SYNTHESIS

Received
21 August 2013

Accepted
27 January 2014

Published
10 March 2014

Correspondence and requests for materials should be addressed to P.F.H. (hpf-hqx@shu.edu.cn)

Engineering the metathesis and oxidation-reduction reaction in solid state at room temperature for nanosynthesis

Pengfei Hu[1], Yali Cao[2], Dianzeng Jia[2], Qiang Li[1] & Ruili Liu[3]

[1]Laboratory for Microstructures, Shanghai University, Shangda Road 99, Shanghai 200444, P. R. China, [2]Institute of Applied Chemistry, Xinjiang University, Urumqi, Xinjiang 830046, P. R. China, [3]Department of Chemical Engineering, School of Environment and Chemical Engineering, Shanghai University, Shangda Road 99, 200444, Shanghai, P. R. China.

It is a long-standing goal to explore convenient synthesis methodology for functional materials. Recently, several multiple-step approaches have been designed for photocatalysts Ag_nX@Ag (X = Cl^-, PO_4^{3-}, etc.), mainly containing the ion-exchange (metathesis) reaction followed by photoreduction in solution. But they were obsessed by complicated process, the uncontrollability of composition and larger sizes of Ag particles. Here we show a general solid-state route for the synthesis of Ag_nX@Ag catalysts with hierarchical structures. Due to strong surface plasmon resonance of silver nanoparticles with broad shape and size, the Ag_nX@Ag showed high photocatalytic activity in visible region. Especially, the composition of Ag_nX@Ag composites could be accurately controlled by regulating the feed ratio of $(NH_2OH)_2 \cdot H_2SO_4$ to anions, by which the performance were easily optimized. Results demonstrate that the metathesis and oxidation-reduction reactions can be performed in solid state at room temperature for nanosynthesis, greatly reducing the time/energy consumption and pollution.

Photocatalytic technology has become an important method to degrade organic pollutants. Recently, Ag-based photocatalyst Ag_nX@Ag-NPs has been attracted much attention due to their photocatalytic activity under visible-light irradiation[1–15]. Firstly, silver nanoparticles (Ag-NPs) demonstrate strong visible absorbance in virtue of the strong localized surface plasmon resonance (LSPR) effect[16–20]. Moreover, due to the low Fermi level (E_F) of Ag-NPs[10,11,21], the photo-excited electrons tend to move to the surface of Ag-NPs, resulting in effective segregation of photo-generated electrons and holes. The recombination of photo-generated electron-hole pairs and photo-reduction of Ag_nX is suppressed. Therefore, Ag-based composite catalysts exhibit higher visible absorbance and stability. Several multiple-steps strategies have been designed to synthesize these hybrid photocatalysts[2,3,5–8,11,12,14,15]. Among these researches, ion-exchange[2,3,5,14,15], liquids-assisted hydrothermal[7], and solvothermal reaction[8,12] were adopted firstly to prepare Ag_nX, and then some Ag^+ ions of as-prepared Ag_nX were converted to Ag via UV irradiation. Furthermore, these multiple-steps methods increased the complexity of the procedures, and the sizes of resultant Ag particles were usually in micron scale, reducing the photocatalytic effectiveness of the materials. Especially the composition of prepared Ag_nX@Ag composites could not be controlled accurately, making it difficult to optimize the performance of the materials.

In the nanosyntheis of functional materials, the exchange (metathesis) reaction and redox reaction are usually adopted. The former is a traditional solution-processed synthesis, while the latter is a process happening in solution, or in solid phase at high temperature. If the synthesis can be achieved in solid state at room temperature (mechanochemistry synthesis), the time/energy consumption and pollution in the synthesis process will be markedly reduced. Featured with convenient and eco-friendly, the room-temperature solid-state chemical synthesis technique has sparked intense research interest of scientists[22–27]. In our previous research[10], AgCl@Ag composite with excellent catalytic activity were prepared by a room-temperature solid-state chemical reaction route. In the present work, the solid-state chemical reaction were expanded to other Ag-based hybrid photocatalysts (such as AgBr@Ag, Ag_2CrO_4@Ag and Ag_3PO_4@Ag, etc.), and a general solid synthesis route for these composites were summarized. The obtained Ag particles exhibited lush LSPR nanostructures, and the composition of Ag_nX @Ag can be easily controlled.

Results

Formation mechanism of composites. The route (I) is described by the following reactions:

$$Ag^+(CH_3COOAg)+X^-(NaX)\rightarrow AgX+CH_3COO^-+Na^+(X=Cl^-,Br^-) \quad (1)$$

$$2Ag^+(CH_3COOAg)+2NH_2OH\rightarrow 2Ag+N_2+2H_2O+2H^+(CH_3COOH) \quad (2)$$

The AgCl and AgBr were formed through the ion-exchange reaction (1) between CH_3COOAg and halides (NaCl, NaBr), meanwhile, some Ag^0 atoms were generated by redox reaction (2) between Ag^+ and low-valent nitrogen atoms in $(NH_2OH)_2{\cdot}H_2SO_4$. The route (II) was designed for the synthesis of feeble-acid insoluble silver salts decorated with Ag-NPs which is summarized from the chemical equations (3)–(5):

$$nAg^+(CH_3COOAg)+nX^-(Na_nX)\rightarrow Ag_nX+nCH_3COO^-+nNa^+\left(X=CrO_4^{2-},\ PO_4^{3-},\ \text{etc.}\right) \quad (3)$$

$$Ag_nX+nH^+(H_2SO_4)\rightarrow nAg^+\left(Ag_2SO_4(\text{slightly soluble})\right)+H_nX \quad (4)$$

$$nAg^++nNH_2OH\rightarrow nAg+n/2N_2+nH_2O+nH^+(H_2SO_4) \quad (5)$$

When $(NH_2OH)_2{\cdot}H_2SO_4$ was added into Ag_nX powders obtained from reaction (3), the succeeding process can be conducted along reactions (4) and (5). This can be explained that H^+ from $(NH_2OH)_2{\cdot}H_2SO_4$ made equal molar amounts of Ag^+ release from the surfaces of Ag_nX particles due to the weak acidity of H_nX, which is similar to the surface etching. Then these Ag^+ were reduced to Ag^0 by the low-valent nitrogen atoms in $(NH_2OH)_2{\cdot}H_2SO_4$, causing the in-situ growth of Ag-NPs on the surfaces of Ag_nX particles.

Characterization of structure, composition, and microstructures. The XRD patterns of different Ag_nX@Ag composites are shown in Fig. 1a. The prepared Ag particles had the face-centered-cubic structure in accordance with the standard JCPDS 89–3722, coexisting with corresponding Ag_nX. In the reaction process, the molar ratio of Ag to Ag_nX in the final products could be controlled by the feed ratio of $(NH_2OH)_2{\cdot}H_2SO_4$ to anion ($a:b$ for (I) or $q:p$ for (II)). Theoretically, the ratio of Ag/Ag_nX should be $2a:b$ and $2q:(p\text{-}2q/n)$ in route (I) and (II), respectively. In addition, similar to our previous work for AgCl@Ag[10], the molar ratio of Ag : Ag_nX were approximately estimated according to the element analysis with X-ray energy dispersion spectrum (EDS) of Ag_3PO_4@Ag, Ag_2CrO_4@Ag, AgCl@Ag, and AgBr@Ag (see Supplementary data, Fig. S1). The results are close to the theoretical value ($2q:(p\text{-}2q/n)$ for Ag_3PO_4@Ag and Ag_2CrO_4@Ag, and $2a:b$ for the other two samples). In order to evaluate the capacity of composition adjustment, a series of AgCl@Ag composites were prepared with different feed ratio of $(NH_2OH)_2{\cdot}H_2SO_4$ to Cl^- ($a:b$ = 1:4 (C-1), 1:6 (C-2), 1:8 (C-3), 1:16 (C-4), respectively). The molar ratios of Ag/AgCl in products were calculated by quantitative analysis of the profile-fitted XRD peaks (Fig. S2). The comparison of theoretical and quantitative calculated ratio of Ag/AgCl is listed in Fig. 1b. It is obvious that the actual composition of AgCl@Ag composites agreed quite well with that of theoretical design, indicating that the method used in the present work could prepare the Ag_nX@Ag composite with accurate composition.

Figs. 2 and S3 show representative SEM images of Ag_nX@Ag composites prepared with room-temperature solid-state chemical reaction. Interestingly, the as-prepared Ag_nX@Ag composites possess fine hierarchical structures like jujube cake, indicating that this method is competent to fabricate Ag_nX@Ag composite structures in high yields. It can be clearly seen from the enlarged SEM images that the large quasi-spherical or flaky Ag_nX particles (*ca.* from hundred nanometers to micron) were evenly covered by Ag-NPs with a wide range of shapes and broad size distribution (*ca.* the size range from several to around one hundred nanometers) (Fig. 2). As a whole, Ag-NPs existed in nearly spherical and rodlike outline with different sizes. Specific to the finer morphology, actually, the spherical objects contain oblate or prolate spheroids (marked by the blue circles in the lower picture of panels a, and b in Fig. 2) with various ratio of major to minor axis (R) and polyhedra (red circles). And the rodlike particles contain nanorods (red arrows), nanorices (blue arrows), and other one-dimensional (1D) objects with different aspect ratio (r). Moreover, the distance between adjacent Ag-NPs on the given area is equivalent to or less than the diameter of particle, even becomes dimer or multimer. As shown in Fig. S3a, the Ag-NPs in Ag_2CrO_4@Ag sample mainly formed spherical objects with small interparticle spacing accompanied by several random aggregates, and some regions approximatively formed a two-dimensional (2D) array of Ag-NPs on Ag_2CrO_4 matrix. Compared with the other three samples, the surface of AgBr matrix carries with the minimum density of Ag-NPs, and the size distribution of Ag-NPs appears large (the diameter of big particles in the range of 100–300 nm, while most of the particles below 40 nm) (Fig. S3b). Furthermore, in all samples, the Ag-NPs are well loaded on the rough surface of Ag_nX particles with two behaviors, adhesion and embedded modes. When the latter

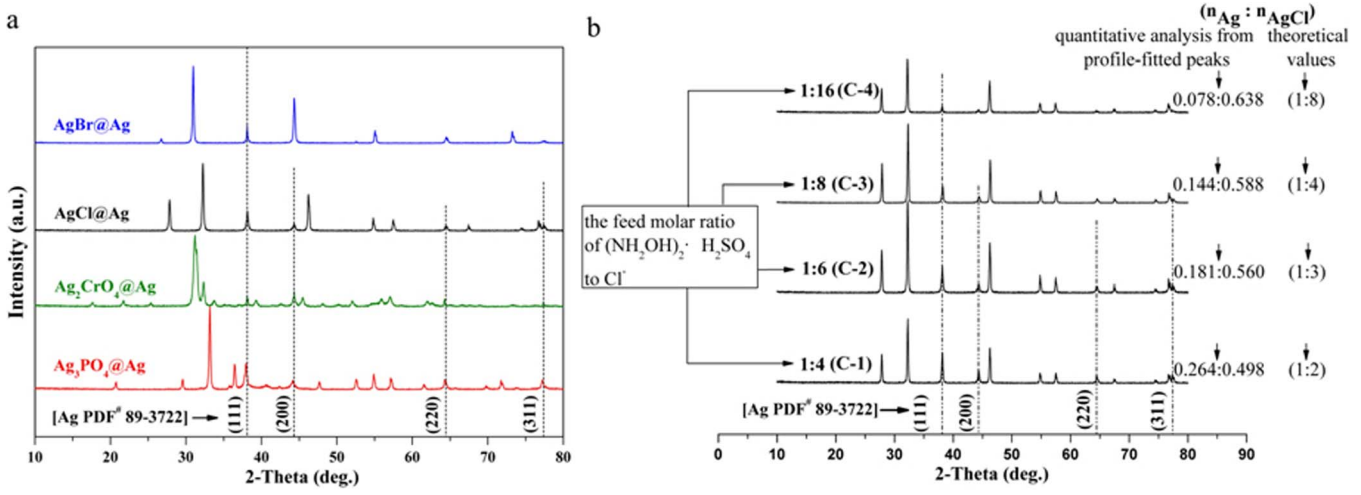

Figure 1 | XRD characterization of Ag_nX@Ag. (a) XRD patterns of Ag_3PO_4@Ag, Ag_2CrO_4@Ag, AgCl@Ag and AgBr@Ag. (b) XRD patterns of AgCl@Ag samples C-1, C-2, C-3, and C-4; and the theoretical and quantitative calculated results.

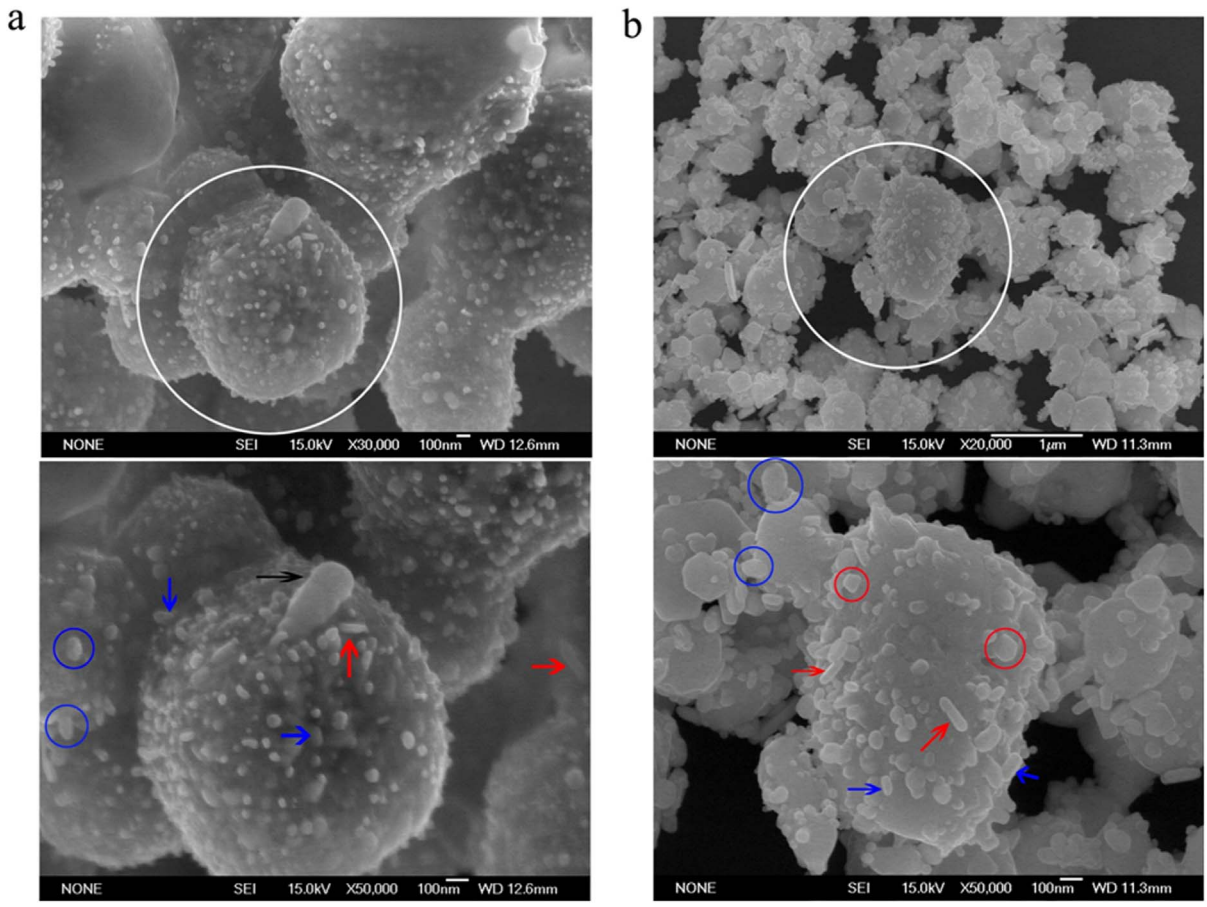

Figure 2 | SEM characterization of Ag_nX@Ag. (a) AgCl@Ag prepared by route (I). (b) Ag_3PO_4@Ag obtained with route (II). The lower image is the high power microscopic view of circle area in the upper. Indications for typical nanostructures: blue circle indicates oblate spheroids, red circle indicates polyhedron, red arrow indicates nanorod, and blue arrows indicates nanorices.

is employed, it is particularly worth noting that the immersion depth in Ag_nX matrix is different. To sum up, the Ag-NPs in the present Ag_nX@Ag composites have following features: (i) the broader size distribution; (ii) the variety of shape, especially, the lower symmetric configuration with different $R(r)$; (iii) the embedded Ag-NPs in the Ag_nX matrix with different immersion depth; and (iv) the small interparticle spacing and random aggregates. In comparison, additionally, the proportion of rodlike and other nonspherical Ag-NPs in Ag_3PO_4@Ag sample and the size is larger than that of the other three samples. This can be attributed to the increasing orientation growth of Ag-NPs in Ag_3PO_4@Ag sample because of the gradual production of metallic silver in the surface etching and regrowth process (due to the moderate-intensity acidity of phosphoric acid). And the Ag-NPs in Ag_2CrO_4@Ag sample show a relatively narrow size distribution than the other three samples. It can be explained that the metallic silver were quickly generated by reaction (4) and (5) due to the weak acidity of chromate (compared to the H_3PO_4), then it adopted instantaneous nucleation growth mode, decreasing the orientation growth.

Attempts have been carried out to observe Ag-NPs by EDS-mapping measurement (under 5 kV accelerating voltage) but it turned out to be unsuccessful (Fig. S4). In accordance with An's report in 2010[4] the spatial distribution and domain morphologies of the Ag-NPs is hard to be clearly imaged with EDS mapping because exposing the Ag_nX@Ag particles to an electron beam with high current density for a long time (for EDS mapping) would constantly reduce part of Ag_nX to metallic silver.

Finally, in order to study the influence of feed ratio ($a:b$) on the product morphology, especially on the shape, size and distribution of Ag-NPs, as well as the resulting different photocatalytic performance, we characterize the samples C-1, 3, and 4 with SEM, UV-Vis spectra, and photodecomposition experiments. Compared with the sample C-2, other samples (C-1, 3, and 4) all display hierarchical structures (Fig. S5). However, between them the density and microstructures of Ag-NPs exist more or less difference. Firstly, the density of Ag-NPs on the surface of AgCl particles increased with the increase of the feed ratio $a:b$ (C-1 > C-2 > C-3 > C-4). The AgCl particles surface in C-4 were sparsely modified with a small amount of Ag-NPs, while the surface of AgCl particles in C-1 is covered by dense Ag-NPs, even stacking. Secondly, the Ag-NPs in C-4 consisted mostly of spheres with various grain sizes ranging from several nanometers to 50 nm, while the other three samples have various formations with broad size distributions (from several to one hundred nanometers) or different $R(r)$, including the patterns of sphere (predominate), nonsphere, and aggregation. Furthermore, with the increasing of feed ratio ($a:b$), considerable large Ag-NPs with a size range of *ca.* 130–250 nm and the aggregation of nanoparticles were generated gradually. In conclusion, the yield of metallic silver increases with the increase of $a:b$, resulting in the increase of the density of Ag-NPs on AgCl particle surface, necessarily, as well the appearance of large and nonspherical particles due to the Ostwald and orientation growth.

UV/Vis absorption and photocatalytic performaces. In order to evaluate the ability of absorbing light in the work environment, we collected the UV-Vis diffuse reflectance spectra (DRS) of samples in the aqueous suspension. Because the photocatalytic tests were carried out in greater than 400 nm light (filtered irradiation ($\lambda > 400$ nm))

and the surface plasmon resonance (SPR) effect of Ag-NPs mostly occurred beyond the wavelength of 300 nm, so we mainly collected and analyzed the DRS at more than 300 nm wavelength of light. Note, the contribution of SPR modes of plasmonic Ag-NPs on the optical absorption of composites and their dependence on particle size, shape, and aggregation state will be discussed latter. Fig. 3a showed that all the samples have strong and broad absorption bands in the visible light region, which can be mainly attributed to the LSPR effects of Ag-NPs, meanwhile, the characteristic absorptions of Ag_3PO_4, Ag_2CrO_4, and AgBr also contribute to the visible light absorption of corresponding composites (direct-bandgap/indirect-bandgap of Ag_3PO_4 and AgBr are 2.43/2.36 eV and 4.28/

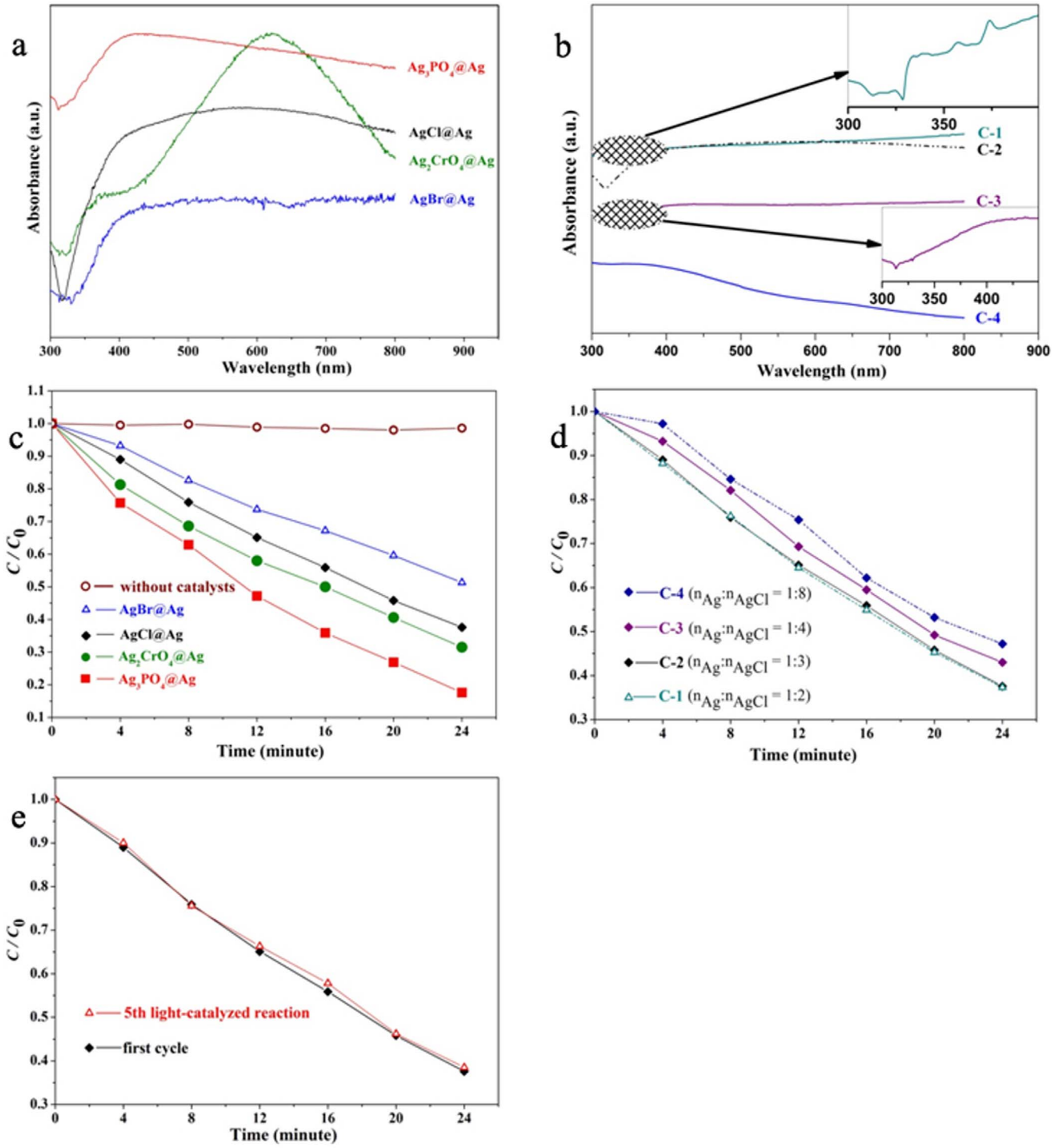

Figure 3 | UV/Vis absorption and photocatalysis characterization of Ag_nX@Ag. (a and b) UV/Vis diffuse reflectance spectra of the as-prepared Ag_3PO_4@Ag, Ag_2CrO_4@Ag, AgBr@Ag, and a series of AgCl@Ag in the aqueous suspension; insets in b are the partial enlarged details of C-1 and C-3 showing the difference in near ultraviolet region. (c) Photodecomposition of methyl orange (MO) without and with the presence of as-prepared Ag_3PO_4@Ag, Ag_2CrO_4@Ag, AgCl@Ag and AgBr@Ag. (d) Photodecomposition of MO over AgCl@Ag samples C-1, C-2, C-3, and C-4. (e) Photodecomposition of MO over AgCl@Ag during the 5th recycling experiment. All photodecomposition experiments were carried out in MO aqueous solution (10 mg·L^{-1}) under visible-light irradiation ($\lambda \geq 400$ nm).

2.46 eV respectively[6,28], band gap of Ag_2CrO_4 is 1.75 eV[29]). To be specific, the Ag_3PO_4@Ag displayed a high energy intense absorption at *ca.* 425 nm followed by a tail of strong absorption pattern extending to 800 nm. It can be deduced that the absorption of Ag_3PO_4 and the LSPR effect of Ag-NPs formed this superimposition spectra, and the absorption edge of Ag_3PO_4 (*ca.* 526 nm) was submerged by total spectra. Similarly, the Ag_2CrO_4@Ag implemented a strong absorption in broad visible region centering at the peak of 615 nm, and coexisting with an obvious absorption shoulder peak at about 360 nm. The AgBr@Ag performed absorption from 400 to 800 nm with a relatively constant output. Moreover, considering the large band gap of AgCl (direct-bandgap/indirect-bandgap is 5.6/3.25 eV[28]), we believe that the visible light absorption of AgCl@Ag is mainly induced by the plasmon resonance of Ag-NPs. In the series of AgCl@Ag products, approximately, the extinction spectrum intensity increased with increasing silver content (but the C-1 and C-2 matched each other) (Fig. 3b). The C-4 DRS spectrum displayed an absorption mound near 370 nm followed with a declined and slightly wavy curve to 800 nm, while other three samples showed absorption in the entire visible region with almost constant intensity. It is worth noting that the C-1 exhibits relatively abundant extinction information in near ultraviolet region (upper illustrations in Fig. 3b).

The photocatalytic activity of the as-prepared catalysts was estimated with the photocatalytic degradation of MO aqueous solution under visible light at room temperature. The relationship between MO-dye decomposition effect and time under visible light irradiation ($\lambda > 400$ nm) of Ag_3PO_4@Ag, Ag_2CrO_4@Ag, AgCl@Ag, and AgBr@Ag composites are shown in Fig. 3c. It should be noted that these four composites had theoretically equal mole ratio of Ag/Ag_nX. The calculated values of MO degradation rate of Ag_3PO_4@Ag, Ag_2CrO_4@Ag, AgCl@Ag, and AgBr@Ag were 0.69, 0.57, 0.52, and 0.41 mg/(min·g_{cat}), respectively. The activities of the latter two samples compare equally or favorably to that of some recently reported corresponding photocatalysts synthesized via other routes[7–9]. And that of Ag_2CrO_4@Ag is slightly weaker than the Huang's report[5]. Moreover, because the photocatalytic measurement of Ag_3PO_4@Ag was carried out with the irradiation wavelength from 400 nm, we cannot develop a parallel comparation of the capacity to other reports which most of them employed the filtered irradiation with wavelengths starting at 420 nm. To ensure objectivity of comparison, we carried out the control experiments with present Ag_3PO_4@Ag under the same conditions of others[13,15]. As shown in Fig. S6, the degradation rate of MO is estimated to be about 0.58 mg/(min·g_{cat}), which is equivalent to that of Ag_3PO_4@Ag in literature 13 (in that case, Ag_3PO_4@Ag $_{AAP\text{-}3}$: 0.56 mg/(min·g_{cat}); Ag_3PO_4@Ag $_{AAP\text{-}2}$: 0.61 mg/(min·g_{cat})). At the same time, a blank experiment revealed that the degradation of MO dye is negligible, where no photocatalyst is used. In current work, we summarized that the photocatalytic ability of catalysts was increased with the increase of the anions' charge ($PO_4^{3-} > CrO_4^{2-} > Cl^-$ (Br^-)). Meanwhile, the photocatalytic ability was also affected by the stability of anions ($Cl^- > Br^-$). This is consistent with the report by Huang and co-workers[5].

Another set of catalytic experiments was carried out to evaluate the photocatalytic ability of C-1, 2, 3, and 4 under visible light at room temperature. As is shown in Fig. 3d, the MO-dye decomposition rate increased with the increase of Ag amount. However, the decomposition capacity was increased slightly when metallic silver reached 20 wt% (molar content 25%). AgCl@Ag composites were then selected as the representative to investigate the stability of the Ag_nX@Ag during the recycling photocatalysis experiment. Fig. 3e shows the photocatalytic activities of recycled AgCl@Ag composites on photocatalytic degradation of MO under visible light. Although AgCl@Ag composites have been re-used for five times, MO molecules were still effectively decomposed at the same constant rate as to the original AgCl@Ag composites. It indicates that the AgCl@Ag composites prepared by room-temperature solid-state reaction demonstrate high photocatalytic stability under visible-light irradiation.

Discussion

It is well known that the silver nanoparticles exhibit LSPR at visible frequencies, which is well understood as a coherent oscillation of the electrons in the local dielectric environment near the surface of metal nanoparticles (NPs). Theoretically and experimentally, the size and shape of the particle as well as the dielectric function of the surrounding medium determine the frequency and the strength of the resonance[30–37]. Furthermore, study on the SPR effect of metal nanoparticle shows that the scattering cross section (SCS) of particles, whose scale is the sixth power of its radius, has great contribution to the extinction efficiency, especially for large nanoparticles (as long as the particles are not large enough to exhibit strong retardation effects). The scattering and absorption of a spherical object with arbitrary size have been described exactly by Mie theory[30,38,39]. Recently, modern numerical calculation techniques including discrete dipole approximation (DDA) method were developed and applied to study the extinction, absorption, scattering, or other optical properties of nonspherical particles, such as oblate spheroid, rod, triangles, prism, and etc.[34,36,37,40,41]. Wherein, Schatz and co-workers[34] described the dipole and quadrupole plasmon resonance of Ag-NPs with a wide range of sizes, shapes, and dielectric environments, and presented a numerical method for calculating extinction and scattering cross-sections in 2003. Results explicitly manifested that the dipolar SPR, whose frequency is generally in the visible light region (except for the very small particles), is particularly sensitive to the particle size, shape, and aspect ratio (one-dimensional/quasi-one-dimensional (1D/quasi-1D) structure). An universal conclusion is that the dipolar SPR wavelength will obviously shift to the red when the size of spherical object or the $R(r)$ of 1D/quasi-1D structure increased, while the frequency of quadrupole component is relatively weak sensitive to above parameters (i.e. the optical intensity changes rapidly while peak position changes slowly) and it can be "quenched" by particle asymmetry.

In the present work, based on the microstructure of Ag-NPs, the behavior of as-prepared Ag-NPs in the UV-Vis spectra can be supported by corresponding DDA theoretical prediction. Firstly, the plasmon resonance energy and width are inherently blurred in bulk measurements because of the inhomogeneity of silver nanoparticles. Here, the Ag-NPs in each Ag_nX@Ag composites all have variable shapes with a broad size distribution or $R(r)$, such as spheroid, polyhedron, rod, and prism. The dipole plasmon resonances of these variform Ag-NPs were inherently excited in respectively specific wavelength region which mostly fall in the range of visible light region, while the quadrupole plasmon resonances were also excited in the higher frequency region for the large particles and 1D/quasi-1D structure. The congregation of these resonances will span the entire visible region extending to the near UV region. However, these resonance frequencies are superimposed on each other, cannot be distinguished well besides the Ag_2CrO_4@Ag. Moreover, the embedded mode of Ag-NPs and the small interparticle spacing (cooperative plasmon mode) as well as random aggregates promote the red-shift of the dipole resonance, which in turn increase the absorption and scattering of visible light[34,42]. Secondly, the SCS of Ag-NPs in Ag_3PO_4@Ag and Ag_2CrO_4@Ag are larger than that in other two composites, because the former two had higher surface density of Ag-NPs or larger Ag-NPs under the equal amount of metallic silver. So, the extinction efficiency of Ag_3PO_4@Ag and Ag_2CrO_4@Ag will be higher than that in the other two samples. Of course, it does not exclude the contribution of characteristic absorption of Ag_3PO_4 and Ag_2CrO_4 in visible region. Furthermore, the small size distribution and small particle spacing of Ag-NPs in Ag_2CrO_4@Ag make the dipole resonance frequency perform in a relatively narrow long

wavelength region interweaving with the characteristic absorption of Ag_2CrO_4, distinguishing the quadrupole resonance peaks.

In analogy to the above analysis, C-1, C-2, and C-3 exhibit excellent absorption in the near UV and visible light regions stemming from the dipole and quadrupole resonances of a great deal of various Ag-NPs, while the C-4 only exist absorption in the near UV and blue light region arisen from the small amount of Ag-NPs and their simplex spherical shape. The gradual increase of extinction intensity along with the increase of metallic silver can be explained as follow: the increase of metallic silver content results in the increase of Ag-NPs surface density, which in turn increases the total SCS. But, after 20 wt% of metallic silver, the new producing metallic-silver is mainly used for several large particles growing, leading to the phase retardation of incident radiation which partially offset the incremental SPR particle contribution. The extinction characters in near UV of C-1 can be attributed to the quadrupole SPR of the unsocial larger particles.

In the present work, rooted in the lush SPR structures of Ag-NPs and the higher composite structure, the prepared Ag_nX@Ag composites showed excellent photocatalytic performances and stability under the visible light irradiation. The Ag-NPs prepared with this method have rich SPR configurations, endowing them with strong ability to capture photon in broad light range (visible), and the absorbed photon would be efficiently decomposed into electron-hole pairs[2,43]. On the one hand, the LSPR could result in enhancement of the local inner electromagnetic field which helps the separation of generated electrons and holes[2]. Additionally, in an Ag_nX@Ag core-shell particle, free electrons in the metallic Ag-NPs are polarized by the Ag_nX core, resulting in regions of negative and positive charges in the Ag-NPs that are far from and close to the Ag_nX/Ag interface, respectively[4]. The polarization field around the Ag_nX core can also force the excited surface electrons in the Ag-NPs further far away from the Ag_nX/Ag interface under illumination while the holes diffuse into the Ag_nX core, namely, the dipolar character of the Ag-NPs make the absorbed photon more efficiently separate to electron-hole pairs[2,4]. As a result, the migration of photo-excited electrons away from the Ag_nX core prevents the recombination of photo-generated electron-hole pairs and photoreduction of Ag^+ to Ag, leading to high activity and stability of the composites. The electrons accumulated on the outer surface of the Ag-NPs can be trapped by O_2 in the water solution to form the reactive oxygen species, such as superoxide ions (O_2^-), while the holes would react with surface hydroxyl groups to form $OH^·$ radicals[2,43,44]. The active species would then degrade the MO.

In the view of excellent SPR structure of Ag-NPs in the Ag_3PO_4@Ag, it had stronger SPR effect in visible irradiation than that of other three samples. Therefore, it would possess stronger photocatalytic activity than that of the others. Other photocatalytic ability sequence can be elucidated by the analyses of microstructure and extinction spectra, for example, that the photocatalytic ability of AgCl@Ag increased with increasing metallic silver content can be ascribed to developing trend of content and the SPR structure of Ag-NPs. Furthermore, according to the study of Huang and co-workers[5], the stability of holes (namely the positive charge centers) determines the activity of photocatalyst, following the rule: the higher stability and higher charged anions lead to the stronger photocatalytic ability. In the present work, better photocatalytic activity of Ag_3PO_4@Ag may due to the high charged PO_4^{3-} anion with high stability and stronger deposited electron ability. Moreover, AgCl@Ag showed higher catalytic ability than AgBr@Ag since the Cl^- is more stable than Br^- (Cl^- is not easy to lost electron compared with Br^-)[5].

In summary, the metathesis and oxidation-reduction reactions were successfully designed in solid state to synthesize a series of Ag_nX@Ag nanophotocatalyts with high activity at room temperature. The composition of Ag_nX@Ag composites could be accurately controlled by regulating the feed ratio of $(NH_2OH)_2·H_2SO_4$ to anions. The Ag-NPs deposited on Ag_nX surfaces have a large number of different shapes and sizes leading to their SPR spectra which cover a wide range of frequencies. And the prepared Ag_nX@Ag composites demonstrated high photocatalytic activity and stability under visible light irradiation. The photocatalytic ability of Ag_nX@Ag composites was affected by the type and stability of anions. And the high amount and stability of charged anions improve the capacity of photocatalyts. The present work suggested a promising green approach for synthesis of functional materials.

Methods

Ag_nX@Ag preparation. The general room-temperature solid-state reaction processes for Ag_nX@Ag are illustrated in Fig. 4. It included the route (I) for silver halides@Ag (strong-acid insoluble silver salts) and the route (II) for Ag_nX@Ag

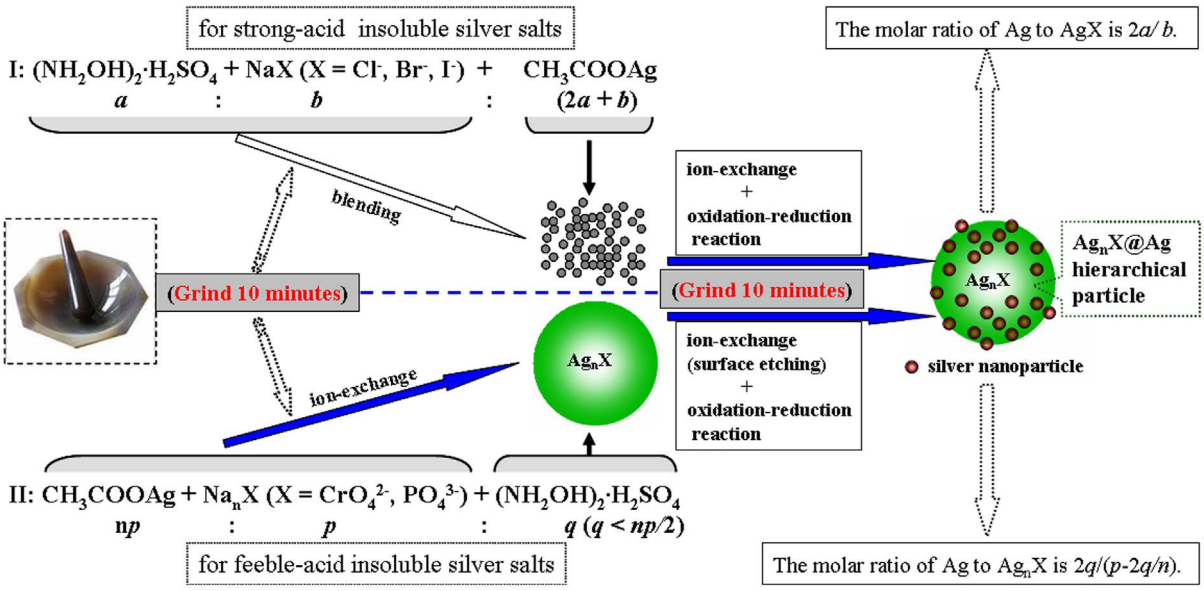

Figure 4 | Schematics of recipe for synthesis of Ag_nX@Ag through room-temperature solid-state reaction process. Ag_nX was formed through the ion-exchange reaction of CH_3COOAg and Na_nX, while metallic silver was generated by redox reaction between Ag^+ and low-valent nitrogen atoms in $(NH_2OH)_2·H_2SO_4$. Theoretically, the malar ratio of Ag/Ag_nX is $2a:b$ in route (I) or $2q:(p\text{-}2q/n)$ in route (II).

(feeble-acid insoluble silver salts). In route (I), powdery $(NH_2OH)_2{\cdot}H_2SO_4$ and halide salts (such as NaCl, NaBr) were mixed with molar ratio of $a:b$, and then the pre-mixture was grounded together for 10 min at room temperature. Afterward, silver acetate (CH_3COOAg) was added into the pre-mixture with absolute molar amount of $(2a + b)$, and this mixture was ground for another 10 min. Finally, the prepared powders were washed with deionized water and dried in air. In route (II), the Ag_nX was firstly obtained by the room-temperature solid-state ion-exchange reaction between CH_3COOAg and soluble salts M_nX (such as Na_2CrO_4, Na_3PO_4, etc.) with feed molar ratio of $np:p$. Then the $(NH_2OH)_2{\cdot}H_2SO_4$ with a given molar amount q (it must be less than 1/2 dose of CH_3COOAg, namely $q < np/2$) was mixed with the collected Ag_nX powder and then grounded for 10 min. Afterward, the mixture was washed with deionized water and dried in air. The resulting powders were washed and dried in air. Then the Ag_nX@Ag sample was characterized by XRD (MXP18AHF, MAC, Cu-Kα $\lambda = 0.154056$ nm), SEM (JSM-6700F), and UV-Vis spectrophotometer (Hitachi U-3310).

Photocatalytic performance. In a typical photocatalytic reaction, 50 mg of the Ag_nX@Ag powder was dispersed in 50 mL aqueous solution of MO (20 $mg{\cdot}L^{-1}$) at room temperature. The mixture was stored in the dark for 1 h to reach the adsorption-desorption equilibrium of MO molecules on the surfaces of photocatalyst particles. A 300 W Xe arc lamp with UV cutoff filter (illuminateing light $\lambda \geq 400$ nm) was used as light source. Under irradiation, about 2 mL suspension was continually taken out from the reaction cell at given time intervals, centrifuging and taking top solution to a quartz cuvette for subsequent MO concentration analysis by monitoring its absorption peak (at 464 nm) intensity with Hitachi U-3310 UV-Vis spectrophotometer (Fig. S7).

The photocatalytic degradation process was denoted by C/C_0, where C_0 is the initial concentration of MO solution (immediately before the ready MO solution over is kept in the dark) and C is the residual concentration at time t (after each period of visible illumination). In the dark, the concentration of the MO-dye has scarcely changed in the dark ($C_{dark}/C_0 \approx 1$), which indicated that the Ag_nX@Ag composite cannot catalyze the decomposition of MO-dye without light irradiation.

1. Elahifard, M. R., Rahimnejad, S., Haghighi, S. & Gholami, M. R. Apatite-coated Ag/AgBr/TiO_2 visible-light photocatalyst for destruction of bacteria. *J. Am. Chem. Soc.* **129**, 9552–9553 (2007).
2. Wang, P. *et al.* Ag@AgCl: A Highly efficient and stable photocatalyst active under visible light. *Angew. Chem. Int. Ed.* **47**, 7931–7933 (2008).
3. Yu, J. G., Dai, G. P. & Huang, B. B. Fabrication and characterization of visible-light-driven plasmonic photocatalyst Ag/AgCl/TiO_2 nanotube arrays. *J. Phys. Chem. C* **113**, 16394–16401 (2009).
4. An, C. H., Peng, S. & Sun, Y. G. Facile synthesis of sunlight-driven AgCl : Ag plasmonic nanophotocatalyst. *Adv. Mater.* **22**, 2570–2574 (2010).
5. Huang, H. *et al.* Tuning metal@metal salt photocatalytic abilities by different charged anions. *Dalton Trans.* **39**, 10593–10597 (2010).
6. Yi, Z. G. *et al.* An orthophosphate semiconductor with photooxidation properties under visible-light irradiation. *Nat. Mater.* **9**, 559–564 (2010).
7. Lou, Z. Z. *et al.* The synthesis of the near-spherical AgCl crystal for visible light photocatalytic applications. *Dalton Trans.* **40**, 4104–4110 (2011).
8. Han, L., Wang, P., Zhu, C. Z., Zhai, Y. M. & Dong, S. J. Facile solvothermal synthesis of cube-like Ag@AgCl: a highly efficient visible light photocatalyst. *Nanoscale* **3**, 2931–2935 (2011).
9. Zhu, M. S., Chen, P. L. & Liu, M. H. Graphene oxide enwrapped Ag/AgX (X = Br, Cl) nanocomposite as a highly efficient visible-light plasmonic photocatalyst. *ACS Nano* **5**, 4529–4536 (2011).
10. Hu, P. F. & Cao, Y. L. A new chemical route to a hybrid nanostructure: room-temperature solid-state reaction synthesis of Ag@AgCl with efficient photocatalysis. *Dalton Trans.* **41**, 8908–8912 (2012).
11. Hou, Y. *et al.* Ag_3PO_4 oxygen evolution photocatalyst employing synergistic action of Ag/AgBr nanoparticles and graphene sheets. *J. Phys. Chem. C* **116**, 20132–20139 (2012).
12. Wang, X. P., Tang, Y. X., Chen, Z. & Lim, T.-T. Highly stable heterostructured Ag-AgBr/TiO_2 composite: a bifunctional visible-light active photocatalyst for destruction of ibuprofen and bacteria. *J. Mater. Chem.* **22**, 23149–23158 (2012).
13. Liu, Y. P. *et al.* One-pot pyridine-assisted synthesis of visible-light-driven photocatalyst Ag/Ag_3PO_4. *Appl. Catal. B-Environ.* **115–116**, 245–252 (2012).
14. Tang, Y. X. *et al.* Efficient Ag@AgCl cubic cage photocatalysts profit from ultrafast plasmon-induced electron transfer processes. *Adv. Funct. Mater.* **23**, 2932–2940 (2013).
15. Gondal, M. A., Chang, X., Sha, W. E. I., Yamani, Z. H. & Zhou, Q. Enhanced photoactivity on Ag/Ag_3PO_4 composites by plasmonic effect. *J. Colloid Interf. Sci.* **392**, 325–330 (2013).
16. Papavassiliou, G. C. Optical properties of small inorganic and organic metal particles. *Prog. Solid State Chem.* **12**, 185–271 (1979).
17. Sherry, L. J., Chang, S. H., Schatz, G. C. & Van Duyne, R. P. Localized surface plasmon resonance spectroscopy of single silver nanocubes. *Nano Lett.* **5**, 2034–2038 (2005).
18. Andrew Murray, W., Suckling, J. R. & Barnes, W. L. Overlayers on silver nanotriangles: field confinement and spectral position of localized surface plasmon resonances. *Nano Lett.* **6**, 1772–1777 (2006).
19. Andrew Murray, W. & Barnes, W. L. Plasmonic materials. *Adv. Mater.* **19**, 3771–3782 (2007).
20. Maier, S. A. *Plasmonics: Fundamentals and Applications.* (Springer, 2007).
21. Henglein, A. & Meisel, D. Spectrophotometric observations of the adsorption of organosulfur compounds on colloidal silver nanoparticles. *J. Phys. Chem. B* **102**, 8364–8366 (1998).
22. Bonneau, P. R., Jarvis, R. F. & Kaner, R. B. Rapid solid-state synthesis of materials from molybdenum disulphide to refractories. *Nature* **349**, 510–512 (1991).
23. Stein, A., Keller, S. W. & Mallouk, T. E. Turning down the heat: design and mechanism in solid-state synthesis. *Science* **259**, 1558–1564 (1993).
24. Ye, X. R., Jia, D. Z., Yu, J. Q., Xin, X. Q. & Xue, Z. L. One-step solid-state reactions at ambient temperatures-a novel approach to nanocrystal synthesis. *Adv. Mater.* **11**, 941–942 (1999).
25. Wang, R. Y. *et al.* Rapid synthesis of amino acid polyoxometalate nanotubes by one-step solid-state chemical reaction at room temperature. *Adv. Func. Mater.* **16**, 687–692 (2006).
26. Lu, J. *et al.* Solid-state synthesis of monocrystalline iron oxide nanoparticle based ferrofluid suitable for magnetic resonance imaging contrast application. *Nanotechnology* **17**, 5812–5820 (2006).
27. Service, R. F. Don't sweat the small stuff. *Science* **320**, 1584–1585 (2008).
28. Tejeda, J., Shevchik, N. J., Brau, W., Goldmann, A. & Cardona, M. Valence bands of AgCl and AgBr: uv photoemission and theory. *Phys. Rev. B* **12**, 1557–1566 (1975).
29. Ouyang, S. X. *et al.* Correlation of crystal structures, electronic structures, and photocatalytic properties in a series of Ag-based oxides: $AgAlO_2$, $AgCrO_2$, and Ag_2CrO_4. *J. Phys. Chem. C* **112**, 3134–3141 (2008).
30. Mie, G. Beiträge zur optik trüber medien, speziell kolloidaler metallösungen. *Ann. Phys.* **330**, 377–445 (1908).
31. Kreibig, U. & Vollmer, M. *Optical Properties of Metal Clusters.* (Springer Series in Materials Science 25, Springer-Verlag: New York, 1995).
32. Link, S. & El-sayed, M. A. Spectral properties and relaxation dynamics of surface plasmon electronic oscillations in gold and silver nanodots and nanorods. *J. Phys. Chem. B* **103**, 8410–8426 (1999).
33. Mock, J. J., Barbic, M., Smith, D. R., Schultz, D. A. & Schultz, S. Shape effects in plasmon resonance of individual colloidal silver nanoparticles. *J. Chem. Phys.* **116**, 6755–6759 (2002).
34. Kelly, K. L., Coronado, E., Zhao, L. L. & Schatz, G. C. The optical properties of metal nanoparticles: the influence of size, shape, and dielectric environment. *J. Phys. Chem. B* **107**, 668–677 (2003).
35. Evanoff, D. D. & Chumanov, G. Size-controlled synthesis of nanoparticles. 1. "Silver-Only" aqueous suspensions via hydrogen reduction. *J. Phys. Chem. B* **108**, 13948–13956 (2004).
36. Wiley, B. J. *et al.* Maneuvering the surface plasmon resonance of silver nanostructures through shape-controlled synthesis. *J. Phys. Chem. B* **110**, 15666–15675 (2006).
37. Wiley, B. J. *et al.* Synthesis and optical properties of silver nanobars and nanorice. *Nano Lett.* **7**, 1032–1036 (2007).
38. Bohren, C. F. & Huffman, D. R. *Absorption and Scattering of Light by Small Particles* (John Wiley & Sons, Inc., 1983).
39. Ringe, E., Sharma, B., Henry, A. I., Marks, L. D. & Van Duyne, R. P. Single nanoparticle plasmonics. *Phys. Chem. Chem. Phys.* **15**, 4110–4129 (2013).
40. Draine, B. T. & Flatau, P. J. Discrete-dipole approximation for scattering calculations. *J. Opt. Soc. Am. A* **11**, 1491–1499 (1994).
41. Mishchenko, M. I., Hovenier, J. W. & Travis, L. D. *Light Scattering by Nonspherical Particles: theory, measurements, and applications.* (Academic Press, San Diego, 2000).
42. Lazarides, A. A. & Schatz, G. C. DNA-linked metal nanosphere materials: Fourier-transform solutions for the optical response. *J. Chem. Phys.* **112**, 2987–2993 (2000).
43. Hoffmann, M. R., Martin, S. T., Choi, W. & Bahnemann, W. Environmental applications of semiconductor photocatalysis. *Chem. Rev.* **95**, 69–96 (1995).
44. Soni, S. S., Henderson, M. J., Bardeau, J. F. & Gibaud, A. Visible-light photocatalysis in titania-based mesoporous thin films. *Adv. Mater.* **20**, 1493–1498 (2008).

Acknowledgments

This work was funded by National Natural Science Foundation of China (21343002), National Nature Science Foundation of China (Grant No.21101132), Shanghai Pujiang Program (11PJ1403600), Program for Professor of Special Appointment (Eastern Scholar).

Author contributions

P.F.H., Y.L.C. and D.Z.J. planned the research. P.F.H., Y.L.C. and Q.L. performed the experiments. P.F.H. and R.L.L. wrote the paper, and all authors discussed the results and commented on the manuscript.

Additional information

Supplementary information accompanies this paper at http://www.nature.com/scientificreports

Competing financial interests: The authors declare no competing financial interests.

How to cite this article: Hu, P.F., Cao, Y.L., Jia, D.Z., Li, Q. & Liu, R.L. Engineering the metathesis and oxidation-reduction reaction in solid state at room temperature for nanosynthesis. *Sci. Rep.* **4**, 4153; DOI:10.1038/srep04153 (2014).